# On the Catalytic Mechanism of ( S )-2-Hydroxypropylphosphonic Acid Epoxidase (HppE): A Hybrid DFT Study

**ARTICLE** *in* CHEMISTRY - A EUROPEAN JOURNAL · JANUARY 2013

Impact Factor: 5.73 · DOI: 10.1002/chem.201202825 · Source: PubMed



**3 AUTHORS**, INCLUDING:

Ewa Broclawik
Polish Academy of Sciences
**154** PUBLICATIONS **1,470** CITATIONS
SEE PROFILE

Tomasz Borowski
Instytut Katalizy i Fizykochemii Powierzchn...
**45** PUBLICATIONS **1,215** CITATIONS
SEE PROFILE

CHEMISTRY
A EUROPEAN JOURNAL

FULL PAPER

DOI: 10.1002/chem.201202825

# On the Catalytic Mechanism of (*S*)-2-Hydroxypropylphosphonic Acid Epoxidase (HppE): A Hybrid DFT Study

**Anna Miłaczewska, Ewa Broclawik, and Tomasz Borowski*[a]**

**Abstract:** The mechanism of oxidative epoxidation catalyzed by HppE, which is the ultimate step in the biosynthesis of fosfomycin, was studied by using hybrid DFT quantum chemistry methods. An active site model used in the computations was based on the available crystal structure for the HppE-$Fe^{II}$-(*S*)-HPP complex and it comprised first-shell ligands of iron as well as second-shell polar groups interacting with the substrates. The reaction energy profiles were constructed for three a priori plausible mechanisms proposed in the literature, and it was found that the most likely scenario for the native substrate, that is, (*S*)-HPP, involves generation of the reactive $Fe^{III}$–O˙/$Fe^{IV}$=O species, which is responsible for the C–H bond-cleavage. At the subsequent reaction stage, the OH-rebound, which would lead to a hydroxylated product, is prevented by a fast protonation of the OH ligand and, as a result, ring closure is the energetically preferred step. For the *R* enantiomer of the substrate ((*R*)-HPP), which is oxidized to a keto product, comparable barrier heights were found for the C–H bond activation by both the $Fe^{III}$–$O_2^{\bullet}$ and $Fe^{IV}$=O species.

**Keywords:** antibiotics · biosynthesis · density functional calculations · epoxidation · iron

## Introduction

The ultimate step in the biosynthesis of fosfomycin, which is a clinically useful antibiotic, is a dehydrogenation reaction in which (*S*)-2-hydroxypropylphosphonic acid ((*S*)-HPP) is oxidatively cyclized to an oxirane-based antibiotic (Figure 1 A). The reaction, catalyzed by (*S*)-2-hydroxypropylphosphonic acid epoxidase (HppE), was characterized for the first time for the *Streptomyces wedmorensis* species and it requires $Fe^{II}$, $O_2$, NAD(P)H, and a flavin coenzyme (FMN or FAD) for activity.[1] The oxidant in the reaction is $O_2$, which is reduced to water with four electrons; two electrons are provided by NAD(P)H and two by the substrate, that is, (*S*)-HPP (Figure 1 A).

Important insights into the mechanism of this unprecedented cyclization reaction were obtained from early isotope labeling experiments performed with culture broths of fosfomycin-producing strains. It was established that the pro-*R* hydrogen bound to C1 of (*S*)-HPP is specifically lost in the reaction,[2] whereas the epoxide oxygen of fosfomycin originates from the OH group of (*S*)-HPP.[3] Other observations made in the same research group are also of mechanistic relevance: First, the *trans*-epoxide epimer of fosfomycin was indirectly identified as a co-metabolite of fosfomycin; (1*S*,2*S*)-1,2-epoxypropylphosphonic acid is produced in 2–3% yield by *Streptomyces fradae* HppE.[4] Second, (*R*)-HPP was shown to be processed by HppE to a keto product, that is, 2-oxopropylphosphonic acid (Figure 1 B) at rate comparable to that for the native reaction.[5] In addition, the 1,1-difluoro derivative of (*R*)-HPP is similarly processed to a keto product, whereas the 1,1-difluoro derivative of (*S*)-HPP was found to be a tight-binding inhibitor of HppE. These results present strong arguments for a mechanism involving C–H bond-cleavage leading to species with, most likely, a radical center at C1 for (*S*)-HPP and at C2 for (*R*)-HPP. In the former, the C2-bound oxygen would subsequently attack the C1 radical forming fosfomycin and an amount of the *trans*-

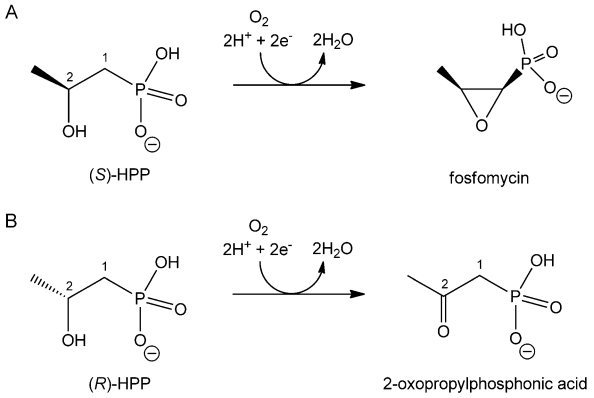


Figure 1. Two reactions catalyzed by HppE: A) cyclization of (*S*)-HPP to fosfomycin; B) oxidation of (*R*)-HPP to a keto product.

[a] A. Miłaczewska, Prof. E. Broclawik, Dr. T. Borowski
Jerzy Haber Institute of Catalysis and Surface Chemistry
Polish Academy of Sciences, ul. Niezapominajek 8, 30-239 Cracow (Poland)
Fax: (+48) 12-4251923
E-mail: ncborows@cyf-kr.edu.pl

Supporting information for this article (including a short summary of CCSD(T) benchmark calculations for $Fe^{III}$–O˙/$Fe^{IV}$=O energy splitting, Cartesian coordinates, calculated energies for all structures, and imaginary frequencies for transition states) is available on the WWW under http://dx.doi.org/10.1002/chem.201202825.

epoxide product through rotation around the C1–C2 bond and subsequent cyclization, whereas the C2-radical derived from (*R*)-HPP would lose one more electron and form the keto product.

Biochemical and spectroscopic studies on HppE provided further data on the reaction and its catalyst. Amongst the various redox-active metals tested, only $Fe^{II}$ is able to reconstitute the activity of an apo enzyme, whereas dioxygen and NAD(P)H are strictly required for the reaction.[6,7] The flavin coenzyme, FMN or FAD, is not an integral part of HppE, yet its presence in the reaction mixture greatly increases fosfomycin production, because it functions as a one-electron mediator between NAD(P)H and HppE. Indeed, flavin cofactors can be replaced with exogenous protein reductase, $E_3$, an NADH-dependent [$Fe_2$–$S_2$]-containing flavoprotein reductase from *Yersinia pseudotuberculosis*, which was shown to be a more effective electron mediator than FMN. EPR studies indicated that (*S*)-HPP binds either in the vicinity or directly to the active site ferrous ion. Moreover, NO, and thus presumably also $O_2$, can bind to the metal in the enzyme–substrate complex.[6]

When HppE is reconstituted with $Fe^{II}$ under aerobic conditions (but in the absence of HPP), a green $Fe^{III}$-catecholate complex forms. The green chromophore results from the oxidation of a tyrosine residue with the most likely site of self-oxidation at Tyr105, as revealed on the basis of resonance Raman and site-specific mutagenesis studies.[8] Thus, HppE can act as oxygenase, forming activated oxygen species, possibly $Fe^{IV}$=O or $Fe^{III}$–OOH, responsible for self-hydroxylation. By extension, the same activated oxygen species may be involved in the catalytic mechanism leading to fosfomycin, in which it would be responsible for C1–H bond activation.[8] Measurements of competitive $^{16}O/^{18}O$ kinetic isotope effects on $k_{cat}/K_m(O_2)$ indicate that the first irreversible step of $O_2$ activation is the catalytic step of HppE, in which the $Fe^{III}$–OOH species is formed.[9]

Valuable information on the binding mode of the substrate within the HppE active site was provided by independent X-ray crystallography and EPR studies. The first crystal structures solved for HppE-$Fe^{II}$-(*S*)-HPP complexes showed that the substrate binds directly to the active site $Fe^{II}$ ion, either as a monodentate or a bidentate ligand.[10] The monodentate binding through an oxygen atom of the phosphonic group is believed to be realized in the intermediate step of HPP binding to the enzyme, because the active site is relatively open at this stage. On the other hand, in the complex featuring the substrate in a bidentate configuration, with C2-bound and phosphonic oxygen atoms ligating $Fe^{II}$, a hairpin fragment of the protein covers the hydrophobic part of the substrate and the active site is closed, which prepares it for further catalytic steps. As shown in Figure 2, one face of the iron coordination octahedron is occupied by two histidines (His138 and His180) and one glutamate (Glu142) side chain, that is, a common motif found in many non-heme iron enzymes.[11] The substrate chelates the ferrous ion with its phosphonic oxygen bound *trans* to Glu142 and the C2-bound oxygen *trans* to His138. The sixth coordination site, *trans* to His180 is empty and it is a suggested place for $O_2$ binding; an activated oxygen species located at this site would have an easy access to the pro-*R* C1-bound hydrogen of (*S*)-HPP that is lost during the catalytic reaction (see above). A recently solved crystal structure for a HppE-$Fe^{II}$-(*S*)-HPP-NO complex (PDB: 3SCF) shows indeed that NO, which is an $O_2$ surrogate, binds *trans* to His180.[12] Moreover, the structure of the HppE-$Fe^{II}$-(*R*)-HPP complex proves that (*R*)-HPP binds to the active site iron in the same fashion as (*S*)-HPP; however, due to its different stereochemistry, the C2-bound hydrogen is exposed towards the activated oxygen species, which is proposed to form at the site *trans* to His180. This structural data is consistent with the results of a previous EPR study, in which $^{17}O$-enriched substrates and substrate analogues were used to probe the substrate binding mode,[13] and showed that the C2-bound OH group is a prerequisite for bidentate binding. In the HppE-$Fe^{II}$-substrate-NO complex, the C2-bound oxygen, the phosphonic oxygen, and NO all bind to the $Fe^{II}$ ion at the same time.

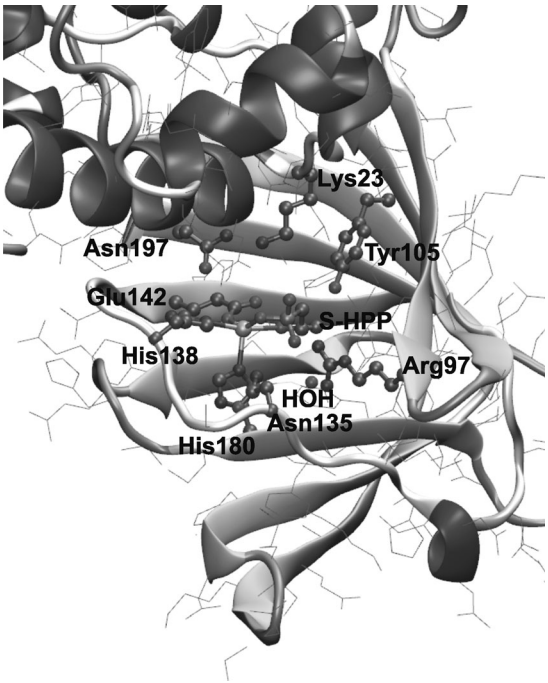


Figure 2. The active site region of the HppE-$Fe^{II}$-(*S*)-HPP complex with bidentate configuration of the substrate (PDB: 1ZZ8). Iron, first-shell ligands, and polar groups from the second coordination shell are ball-and-stick representations. Figure prepared with the VMD program.[31]

In the second coordination shell there are several polar residues forming hydrogen bonds with the phosphonic group of the substrate (Figure 2). Basic nitrogen atoms of Lys23 and Arg97 are placed around 3.4 Å away from phosphonic oxygens of (*S*)-HPP, whereas the distances between phosphonic oxygens and Tyr105 hydroxo oxygen and Asn135 amid nitrogen are 2.7 and 2.9 Å, respectively. A single water molecule also forms a hydrogen bond with the $PO_3$ group (oxygen–oxygen distance of ca. 2.6 Å).

  

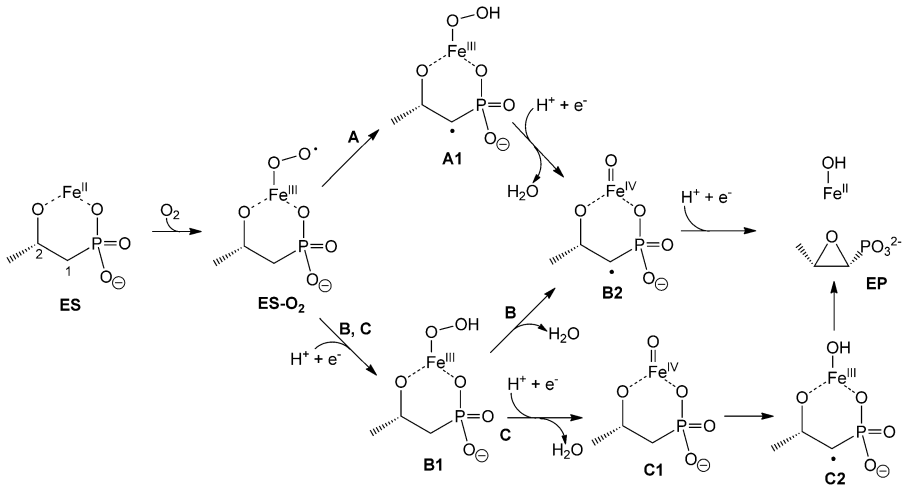


Figure 3. Three reaction mechanisms proposed for HppE: A) $Fe^{III}$-bound superoxide responsible for the C–H bond cleavage; B) $Fe^{III}$-bound hydroperoxo group responsible for the C–H bond cleavage; C) $Fe^{IV}$=O activating the C–H bond.

The results of the above summarized studies allowed for formulation of plausible reaction mechanisms for the oxidative cyclization reaction catalyzed by HppE, which are shown in Figure 3.[1,5,7,8,10,13] In each of the three mechanisms (**A**–**C**), an activated oxygen species abstracts the C1-bound hydrogen atom forming a C1-based radical (**A1**, **B2**, or **C2**). Subsequently, the C1-radical forms a bond with the C2-bound oxygen and yields the expoxide ring of fosfomycin (**EP**). The mechanisms differ by the identity of the activated oxygen species and by the stage when the two electrons from NAD(P)H are delivered to the active site through a one-electron mediator. Thus, in mechanism **A**, it is the superoxide present in the **ES-O$_2$** complex that activates the C1–H bond (**ES-O$_2$**→**A1**), and the electrons and protons, necessary for full reduction of dioxygen to water are delivered in two subsequent steps (**A1**→**B2**, **B2**→**EP**). In mechanism **B**, the superoxo **ES-O$_2$** complex is first reduced by one electron and then protonated to form a $Fe^{III}$–OOH species (**B1**) that activates the C1–H bond through homolytic O–O bond cleavage (**B1**→**B2**). In mechanism **C**, the O–O bond is cleaved prior to the C1–H bond activation as two electrons and two protons are consumed to form the reactive $Fe^{IV}$=O species (**ES-O$_2$**→**B1**→**C1**) responsible for the cleavage of the C–H bond (**C1**→**C2**). Each of the mechanisms has some precedence in the chemistry of non-heme iron systems. More specifically, $Fe^{III}$-bound superoxide is responsible for the C–H bond cleavage in the reactions catalyzed by isopenicillin *N*-synthase, *myo*-inositol oxygenase, and hydroxyethylphosphonate dioxygenase (HEPD), a situation analogous to mechanism **A**.[14,22] A $Fe^{III}$–OOH form of an anticancer drug bleomycin was proposed to be responsible for a C–H cleavage reaction, analogous to the **B1**→**B2** step.[15] Note, however, that the activated bleomycin is a low-spin complex, whereas $Fe^{III}$ in HppE has most likely a high-spin configuration, which may affect the reactivity of this species.[16] Finally, the activation of an aliphatic C–H bond by the $Fe^{IV}$=O species (mechanism **C**) is encountered in various biosynthetic routes catalyzed by non-heme iron enzymes.[17,18]

The present contribution describes a computational study undertaken with the aim to provide energetics data on the three alternative mechanisms depicted in Figure 3. Hybrid DFT method B3LYP, and its derivative B3LYP*, was applied to an active site model to construct reaction energy diagrams for critical steps of the three mechanisms. Most importantly, it was found that mechanism **C** is most likely responsible for HppE catalyzed cyclization of (*S*)-HPP to fosfomycin. On the other hand, oxidation of (*R*)-HPP to the keto product (Figure 1B) may proceed either along mechanism **A** or mechanism **C**. A detailed description of the computational models and methods and discussion of the obtained results are provided in the following sections.

## Results and Discussion

**Mechanism A: $Fe^{III}$–$O_2^{\bullet}$ activating the C1–H bond of (*S*)-HPP**: The first step common to all three mechanisms is the binding of dioxygen to the HppE-$Fe^{II}$-(*S*)-HPP complex (**ES**; Figure 3). With three negatively charged ligands in the first coordination shell (Glu142, (C2-)O and $PO_3$ groups of HPP), $Fe^{II}$ in the **ES** complex is expected to possess substantial electron density, and thus, activated for binding electrophilic $O_2$. Indeed, the calculated energy of $O_2$ binding to form the $Fe^{III}$–$O_2^{\bullet}$ species in the septet ground state ($^7$**2**) is substantial; equal to $-6.1$ kcal mol$^{-1}$ (see later, Figure 5). The same effect calculated without vdW and ZPE corrections is still $-0.5$ kcal mol$^{-1}$, which is 4.3 kcal mol$^{-1}$ more favorable than the value computed for an α-ketoacid-dependent enzyme featuring two negatively charged ligands in the $Fe^{II}$ first coordination shell.[19] Besides the ground-state septet ($^7$**2**) and the low-lying quintet state ($^5$**2**, Figure 4A), the triplet- and singlet spin states were optimized for the $Fe^{III}$–$O_2^{\bullet}$ complex, however, they lie 17.0 and 18.2 kcal mol$^{-1}$ higher than the ground state, respectively (the values computed with B3LYP* are 15.1 and 14.5 kcal mol$^{-1}$, respectively). Such an arrangement of spin states, with septet and quintet being close in energy and one of them being the ground state is typical for $Fe^{III}$–$O_2^{\bullet}$ complexes encountered for non-heme iron enzymes with a 2-His-1-carboxylate binding motif.[20–22] Interestingly, a totally different spin-state arrangement was found for cysteine dioxygenase (CDO), in

  

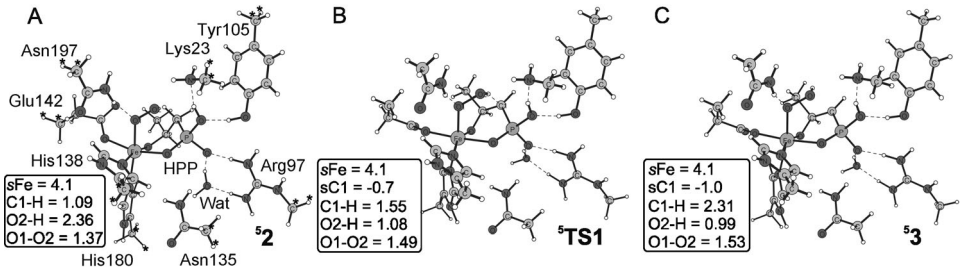


Figure 4. The key structures optimized for the initial steps of mechanism **A**. Atoms marked with asterisks in part A were not allowed to move during geometry optimizations.

which the singlet is the ground state, although in CDO iron is bound by 3-His binding motif, a fact that may be responsible for the difference in spin-state ordering.[23, 24]

In the active sites of mononuclear non-heme iron enzymes the septet spin state of $Fe^{III}$–$O_2^{\bullet}$ is usually not optimal for the progress of the reaction, because it does not allow for a two-electron reduction of $Fe^{III}$–$O_2^{\bullet}$ to $Fe^{II}$–OO–R.[20] However, the reaction in question, that is, **ES-$O_2$→A1** (Figure 3), is a one-electron redox process, and hence it could proceed both on the usually preferred quintet and the septet surfaces. In the former case, **A1** features a high-spin $Fe^{III}$ antiferromagnetically coupled to the C1-centred radical, whereas in the septet state the two sites with unpaired electrons are coupled ferromagnetically. As can be noticed in Figure 5, the C1–H cleavage involves slightly lower barri-

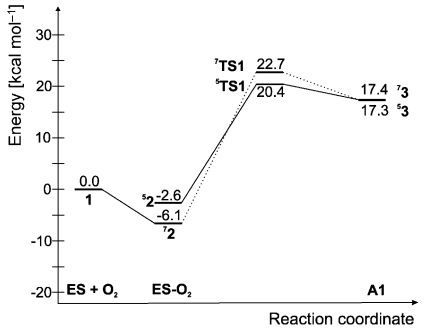


Figure 5. The energy profile computed for the initial steps of mechanism **A**. The solid line marks the lowest energy path. The energy combines electronic energy computed with B3LYP and triple dzeta basis, vdW corrections, solvation energies, and ZPE computed at the B3LYP/lacvp level.

er on the quintet energy surface than on the septet one, however, in both cases the barriers are quite high, that is, 26.5 and 28.8 kcal mol$^{-1}$ for the quintet- and septet spin states, respectively. A very similar barrier height (30.3 kcal mol$^{-1}$ without ZPE correction) was previously found for an analogous step of the catalytic reaction of hydroxyethylphosphonate dioxygenase (HEPD), that is, an enzyme processing a phosphonic substrate very similar to HPP.[22] Moreover, in HEPD the septet and quintet transition-states for the C–H cleavage have, like in HppE, very similar energies.

The barriers computed with the B3LYP* are very similar, that is, 25.8 and 28.2 kcal mol$^{-1}$, which suggests that the results are stable with respect to the choice of the functional. The reaction is considerably endothermic, with reaction energy of +23.4 kcal mol$^{-1}$, and consistently, the transition state has a late character, with the hydrogen atom very close to the destination oxygen (O2; see Figure 4B). The C1–H cleavage product (**3**) was also optimized in the triplet spin-state (low spin $Fe^{III}$ ferromagnetically coupled to the C1-centred radical), however, the $^3$**3** species lies by 14.2 kcal mol$^{-1}$ (B3LYP*: 11.6 kcal mol$^{-1}$) higher than $^5$**3**. Since the two radical centers ($Fe^{III}$ and C1 radical) are well separated in space, it is expected that the singlet state (with antiferromagnetic coupling between $Fe^{III}$ and the C1-radical) will be degenerate with this triplet. Taking into account the very high energies of $^3$**3** and $^1$**3**, it seems safe to conclude that neither triplet nor singlet can take an active role in the studied process.

From the values of Fe spin populations and O1–O2 distance reported in Figure 4, one can notice that in the initial steps of mechanism **A** iron provides one electron to reduce dioxygen to a superoxide radical, and then the latter abstracts the C1-bound hydrogen and reduces to a hydroperoxo group, whereas the $Fe^{III}$ oxidation state is preserved during the **ES-$O_2$→A1** reaction. Thus, one can argue that the high activation barrier and reaction energy connected with this step can be attributed to the relatively low value of the OO–H bond energy compared with that of (HPP)C1-H. Indeed, the bond energies computed with the current methods for HOO-H and (HPP)C1-H amount to 81.0 and 97.4 kcal mol$^{-1}$ for B3LYP and 81.4 and 97.7 for B3LYP*, respectively.

Steps following the C1–H bond activation in mechanisms **A**, for example, **A1→B2**, were not studied, since the energy barriers obtained for mechanism **C** were much more favorable than those described above for the initial steps of mechanism **A** (see below).

**Mechanism B: $Fe^{III}$–OOH activating the C1–H bond of (*S*)-HPP**: The key difference between the mechanisms proposed for HppE is the identity of the activated oxygen species responsible for the C1–H bond cleavage. In mechanism B it is the $Fe^{III}$–OOH species (**B1** in Figure 3) that is involved in this process and it is obtained by one electron and one proton uptake by **ES-$O_2$**. An analogous $Fe^{III}$–OOH species was suggested to be a so-called second oxidant in heme systems (cytochrome P450).[25, 26]

As shown in Figure 6, in the ground state the **B1** species assumes a high-spin $Fe^{III}$ configuration ($^6$**4**) with the lowest-lying excited state being the intermediate spin quartet state ($^4$**4**). The computed energy of a doublet (low spin) state is

  

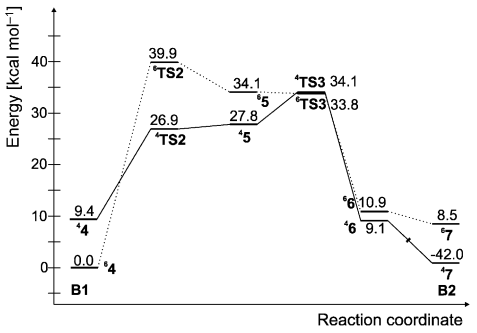


Figure 6. The energy profile computed for the initial steps of mechanism **B**. The solid line marks the lowest energy path. The energy combines electronic energy computed with B3LYP and triple dzeta basis, vdW corrections, solvation energies, and ZPE computed at the B3LYP/lacvp level.

by 15.4 kcal mol$^{-1}$ (B3LYP*: 11.6 kcal mol$^{-1}$) higher than the ground state sextet. The $^{6}$**4**-$^{4}$**4** energy gap is 9.4 kcal mol$^{-1}$ with B3LYP and 6.9 kcal mol$^{-1}$ with B3LYP*, and since the splitting is not large, the mechanism of the **B1**→**B2** step (Figure 3) was studied on both potential energy surfaces (PESs), that is, sextet and quartet.

In the quartet state a transition state for O–OH bond cleavage ($^{4}$**TS2**) was optimized, as was the structure of a resulting intermediate ($^{4}$**5**) with a very stretched O–OH bond (2.50 Å long), yet the computed corrections to the electronic energy put $^{4}$**5** slightly above $^{4}$**TS2**, which indicates that the true transition-state of the **B1**→**B2** step is connected with the C1–H bond cleavage, that is, $^{4}$**TS3** shown in Figure 7 B. In $^{4}$**TS3** the FeO–OH distance is 2.73 Å, whereas the Fe–O bond has a length typical for an oxoferryl species (1.65 Å),[27] which indicates that the O–OH bond is already cleaved at this point of the reaction. Thus, the C1–H bond is activated by the OH radical derived from the leaving OH group. The hydrogen atom being abstracted is located somewhat closer to the O2 atom (1.23 Å) than to the parent C1 (1.29 Å), which is consistent with the fact that the $^{4}$**5**→$^{4}$**6** transition is an exothermic process ($^{4}$**6** corresponds to **B2** with $H_2O$ still bound in the active site). However, the most important observation is that the barrier to the concerted yet asynchronous O–OH and C1–H bonds cleavage ($^{4}$**TS3**) is very high, with B3LYP and B3LYP* values of 34.1 and 28.2 kcal mol$^{-1}$, respectively. Generation of the C1-centred radical involves considerably lower barriers in mechanism **C** (see below) and hence we consider mechanism **B** to be very unlikely.

On the sextet PES the cleavage of the O–OH bond is the rate-limiting step connected with a prohibitively high barrier of 39.9 kcal mol$^{-1}$ (42.5 kcal mol$^{-1}$ with B3LYP*), whereas the subsequent C1–H cleavage by the OH radical ($^{6}$**TS3**) proceeds without any barrier. Quartet and sextet variants of **TS3** are practically degenerate because spin coupling between the Fe$^{IV}$=O and OH/C1 radical sites is very weak due to their considerable spatial separation (see Figure 7 B). The resulting species $^{6}$**6** features Fe$^{IV}$=O and a C1-centred radical as well as a water molecule whose release to the bulk leads to $^{6}$**7**, which is equivalent to **B2**. In the latter species, the distance between the oxo O1 atom and the radical C1 is only 2.83 Å, which suggests the attack of the oxo group on the radical should be a straightforward process. Indeed, on the quartet surface, in which the oxo and the C1 atoms have spin populations of opposite polarization, the bond between the two atoms forms spontaneously once the C1–H bond has been cleaved. Thus, in the structure of the species $^{4}$**7**, in which Fe$^{III}$ is in a spin intermediate state, there is a bond between C1 and O1 that is not present in $^{6}$**7**. Such a spontaneous hydroxylation of C1 is one more argument against mechanism **B**, since former studies on HppE ruled out mechanisms involving C1 hydroxylation.[5]

At this point it should be emphasized that all our attempts to locate transition states for concerted and (more) synchronous O–OH and C1–H cleavage failed to give structures different from the one described above, and hence we conclude that the C1–H bond activation according to mechanism **B** requires the O–OH bond to be already cleaved.

**Mechanism C: Fe$^{IV}$=O activating the C1–H bond of (*S*)-HPP**: In mechanism **C**, which we found to be most probable, the C1–H bond is cleaved by the oxoferryl species (**C1** in Figure 3) produced by the two-electron reduction of the **ES-O$_2$** adduct (and uptake of two protons), and the following O–O bond heterolysis. When modeling a structure of a species obtained by a one electron and proton uptake by **B1**, the incoming proton can be placed on several atoms, that is, the oxygen of the HOO group proximal to the iron (O1), the nitrogen atom of Lys23 and the oxygen of HPP bound to C2. The latter option gave the lowest energy structure, that is, $^{5}$**8** ($^{3}$**8** is by 17.0 kcal mol$^{-1}$ (B3LYP*: 14.4 kcal mol$^{-1}$) less stable), and also led to a low barrier mechanism presented in detail in Figure 8. The corresponding energy di-

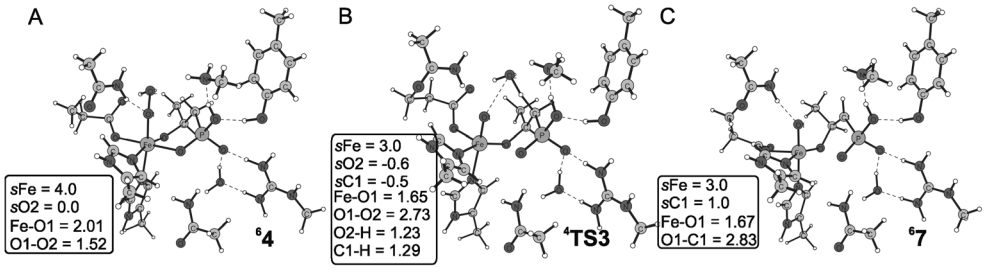


Figure 7. The key structures optimized for the initial steps of mechanism **B**.

  

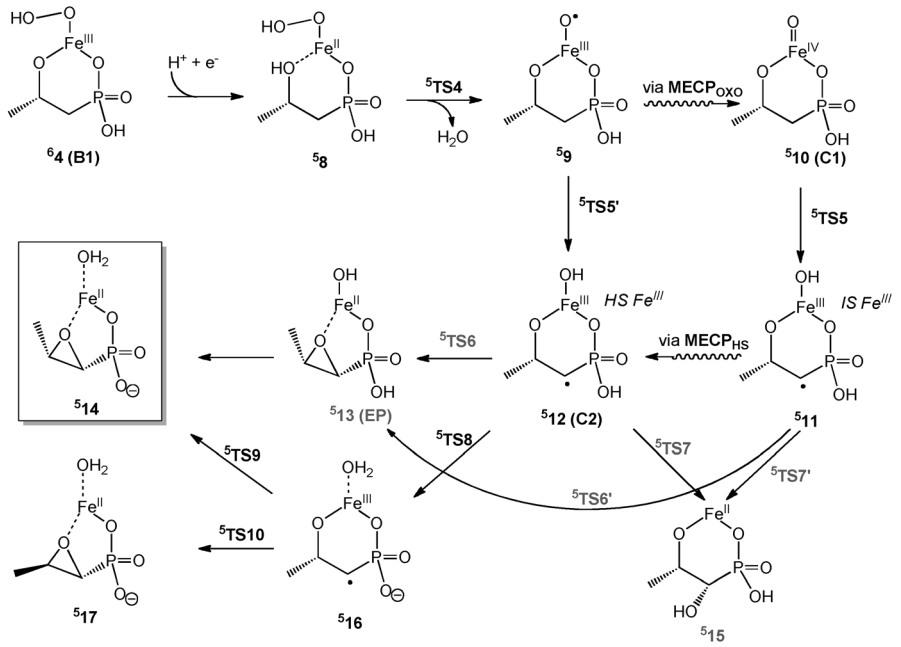


Figure 8. A detailed picture of mechanism **C**. Species with black labels define the most likely mechanism; species with gray labels are higher-energy structures. Fosfomycin-HppE product complex ($^5$**14**) shown within a frame.

agram is shown in Figure 9, whereas the structures of the critical stationary points are depicted in Figure 10 and Figure 11. Cleavage of the O–O bond ($^5$**8**→$^5$**9**) proceeds through $^5$**TS4**, located 12.5 kcal mol$^{-1}$ above the reactant $^5$**8**, and whose structure (Figure 10B) indicates that breaking of the O–O bond is coupled to a proton transfer from the hydroxyl group of HPP to the leaving OH. Interestingly, the product of this step is a metastable species with high-spin Fe$^{III}$ and an oxyl radical whose unpaired electron is located in the 2p orbital perpendicular to the Fe–O bond ($^5$**9**; note the 1.96 Å bond length for Fe–O and large negative spin on O1 in Figure 10C).[28] This species is an excited state form of the usual oxoferryl species ($^5$**10**); the energy gap computed with B3LYP is 18.6 kcal mol$^{-1}$, whereas with B3LYP* it is 24.8 kcal mol$^{-1}$. Benchmark computations with the CCSD(T) method applied to a small model of the iron cofactor (for details, see the Supporting Information) indicate the actual energy separation between $^5$**9** and $^5$**10** is roughly in between these two values, that is, approximately 22 kcal mol$^{-1}$. Such an energy gap would normally exclude the excited state from participation in the reaction, however, in this case the $^5$**9** species is produced directly in the O–O cleavage step and not through excitation form the ground state oxoferryl. Thus, the relative rates of a de-excitation to $^5$**10**, through the minimum energy crossing point (**MECP$_{oxo}$**), and the C1–H cleavage ($^5$**9**→$^5$**TS5′**→$^5$**12**) will be decisive for the choice of the reaction channel for the C1–H cleavage step. **MECP$_{oxo}$** connecting diabatic surfaces on which $^5$**9** and $^5$**10** lay was optimized, yet its energy is basically identical to that for $^5$**9**, which indicates there is no structural barrier to the de-excitation of $^5$**9** to $^5$**10**. On the other hand, in $^5$**9** the pro-*R* hydrogen bound to C1 is only 2.04 Å away from the oxyl radical (Figure 10C) and there is no barrier connected with $^5$**TS5′**. Since in the latter reaction heavy atoms move very little (compare $^5$**9** and $^5$**TS5′** in Figure 10), we speculate that at least part of the reaction flux will flow on the excited state surface ($^5$**9**→$^5$**TS5′**) directly to $^5$**12**, which is a ground state form of the species C2 (Figure 3).

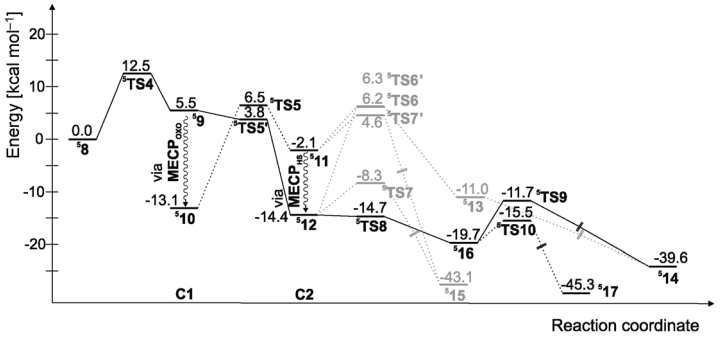


Figure 9. The energy profile computed for mechanism **C**. The solid-line profile marks the most efficient route to fosfomycin; gray steps involve higher activation barriers. The energy combines the electronic energy computed with B3LYP and triple dzeta basis, vdW corrections, solvation energies, and ZPE computed at the B3LYP/lacvp level.

De-excitation of $^5$**9** to $^5$**10** requires that the singly occupied 2p orbital of the oxyl ligand rotates form the perpendicular orientation with respect to the Fe–O bond to the parallel one. As a result a regular Fe=O bond forms, by approximately 0.3 Å shorter than the Fe$^{III}$–O$^{\bullet}$ one.

The C1–H bond cleavage by the ground state oxoferryl species ($^5$**10**) is an example of a relatively rarely observed reactivity in which the substrate is positioned in the active site so that it can approach the Fe=O group only at angles (Fe-O–substrate) close to 90°.[19, 28, 29] This constraint forces the oxoferryl to use its π-orbitals for reaction with the substrate, which in turn leads to a product in an excited state featuring spin intermediate Fe$^{III}$.[28, 29] This is indeed what happens in the $^5$**10**→$^5$**TS5**→$^5$**11** step involving a barrier of 19.6 kcal mol$^{-1}$ (20.8 kcal mol$^{-1}$ with B3LYP*) and being endothermic by 11.0 kcal mol$^{-1}$ (14.3 kcal mol$^{-1}$ with B3LYP*) due to the intermediate spin configuration of Fe$^{III}$ in $^5$**11**. De-excitation of $^5$**11** to the ground state $^5$**12** can proceed through a crossing point **MECP$_{HS}$**, which has a geometry very close to that of $^5$**11** and energy only by 0.3 kcal mol$^{-1}$ higher than $^5$**11**. Inspection of the energy diagram (Figure 9)

  

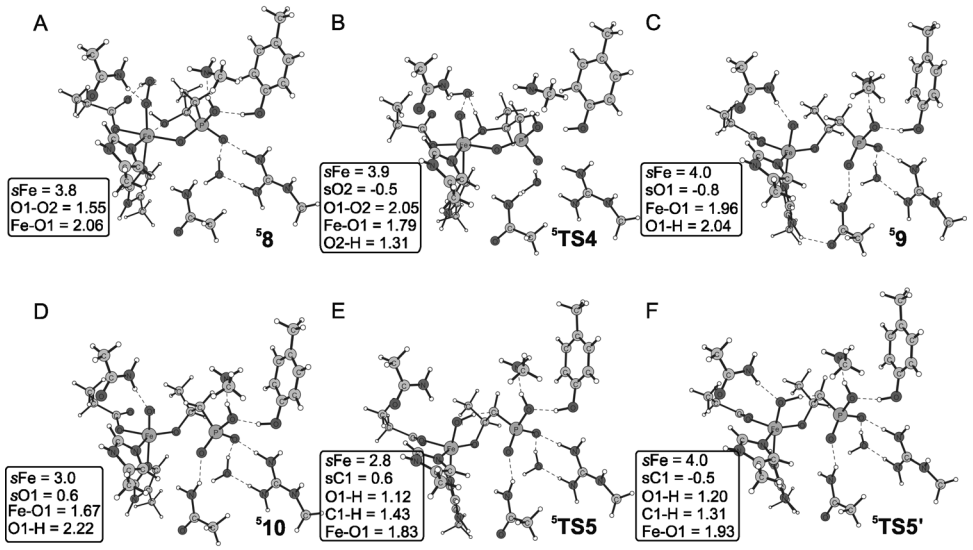


Figure 10. The key structures optimized for the initial steps of mechanism **C**.

reveals that barriers to hydroxylation (**$^5$TS7′**) or cyclization (**$^5$TS6′**) reactions involving **$^5$11** are substantially larger than the 0.3 kcal mol$^{-1}$ barrier connected with **MECP$_{HS}$**, and thus one can safely conclude that the exclusive "reaction" of **$^5$11** is the thermal decay to **$^5$12**.

The "typical" reaction performed by the oxoferryl species is hydroxylation of an organic substrate, which in our case would mean a transfer of the OH group bound to Fe$^{III}$ in species **$^5$12** to the radical carbon C1. Such a step involves a modest barrier of 6.1 kcal mol$^{-1}$ (4.4 kcal mol$^{-1}$ with B3LYP*) connected with **$^5$TS7** and it is practically irreversible as the hydroxylated product **$^5$15** lies 28.7 kcal mol$^{-1}$ (27.8 kcal mol$^{-1}$ with B3LYP*) below the radical intermediate **$^5$12**. The desired cyclization reaction of **$^5$12** can hardly compete with the hydroxylation because its transition state **$^5$TS6** is located 14.5 kcal mol$^{-1}$ higher in energy (14.5 kcal mol$^{-1}$ with B3LYP*) than **$^5$TS7**. However, the Fe$^{III}$-bound hydroxyl group in **$^5$12** is relatively basic, which makes a proton transfer from the $PO_3H$–Lys23 hydrogen-bonded pair (**$^5$12**→**$^5$TS8**→**$^5$16**) an efficient and energy-downhill step. This proton transfer not only prevents the OH-rebound reaction, but also reduces the number of negatively charged ligands in the iron first coordination sphere, from four (in **$^5$12**) to three (in **$^5$16**, see Figure 11 A), which substantially helps in reducing the iron from Fe$^{III}$ to Fe$^{II}$ during formation of the epoxide ring. Indeed, the calculated barrier to ring closure: **$^5$16**→**$^5$TS9**→**$^5$14** amounts to only 8.0 kcal mol$^{-1}$ (6.5 kcal mol$^{-1}$ with B3LYP*), which should be compared with the barrier of 20.6 kcal mol$^{-1}$ (18.9 kcal mol$^{-1}$ with B3LYP*) connected with the **$^5$12**→**$^5$TS6**→**$^5$13** step.

Analysis of structures and spin populations presented in Figure 11 reveals that at the transition state **$^5$TS9** the C1–O3 distance amounts to 1.99 Å, and roughly 0.4 charge is transferred from C1 to iron. In the reaction product **$^5$14**, spin population on Fe has a value typical for high-spin Fe$^{II}$ complexes (3.7), the newly established bond is 1.50 Å long (the other C–O epoxide bond has a length of 1.51 Å), and the epoxide oxygen (O3) has its coordination bond to iron elongated to 2.53 Å. The optimized geometry of the product complex **$^5$14** compares well with the crystal structure solved for the HppE-Zn-fosfomycin complex.[30] The active site region of the crystal structure (PDB: 2BNN) superimposed with **$^5$14** is shown in Figure 12, in which it can be noticed that the placement of the product and its interactions with the active site are very similar in the two structures.

In the present computational model, the side chains of HppE that form a hydrophobic niche for the methyl group of the substrate were not included, which was a necessary simplification for this study in which many transition states and intermediates needed to be characterized. The drawback of this choice, though relatively minor, is that with the present model, a ring-closing reaction leading to an epimer of fosfomycin, that is, the *trans*-epoxide **$^5$17**, has a barrier by 3.8 kcal mol$^{-1}$ (4.0 kcal mol$^{-1}$ with B3LYP*) lower than that connected with formation of fosfomycin (compare **$^5$TS10** and **$^5$TS9** in Figure 9), which means that the *trans*-epimer should be the major product. Experimental results indicate that the latter can be a minor product, and the more crowd-

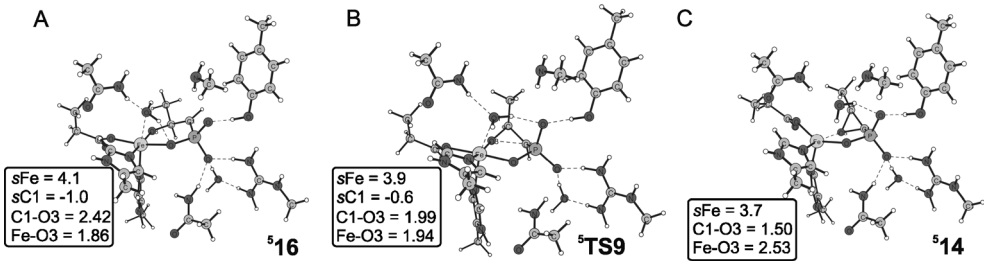


Figure 11. The key structures optimized for the cyclization stage of mechanism **C** leading to fosfomycin.

  

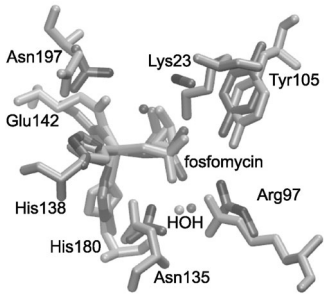


Figure 12. Superimposed structures of: the active site region of the HppE-Zn-fosfomycin complex (PDB: 2BNN), and optimized geometry of the model for HppE-$Fe^{II}$-fosfomycin complex ($^5$**14**). For clarity, hydrogen atoms are not shown. Figure prepared with the VMD program.[31]

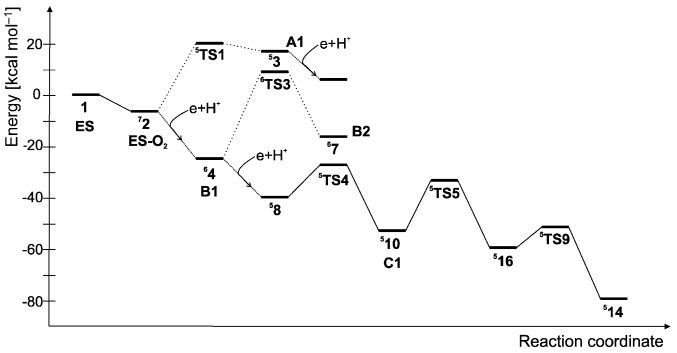


Figure 13. The schematic energy diagram for mechanisms **A**, **B** and **C** including the proton and electron uptake steps. For mechanism **C** the worst case scenario (the largest barrier for the C–H cleavage step) is presented. The energy combines electronic energy computed with B3LYP and triple dzeta basis, vdW corrections, solvation energies, and ZPE computed at the B3LYP/lacvp level.

ed, and thus less stable, *cis*-epoxide-fosfomycin is the major product of the reaction catalyzed by HppE. Thus, it can be argued that the groups not included in the present model are responsible for tuning relative barrier heights connected with $^5$**TS10** and $^5$**TS9**, by approximately 5–6 kcal mol$^{-1}$, so that $^5$**TS9** is located 1–2 kcal mol$^{-1}$ below $^5$**TS10**, and as a result, fosfomycin is the major product. Future computational studies employing more complete models of HppE will verify this hypothesis.

**Energy profiles including electron- and proton-uptake steps**: In the preceding discussion of the energy profiles for mechanisms **A**–**C** the energies of species **1**, $^6$**4**, and $^5$**8** were used as reference points (zeros). This choice is useful when concentrating on the chemical steps of the mechanisms, yet the final energy profile should take into account the energies connected with the delivery of two electrons and two protons to the active site of HppE. In other words, the energies of $^6$**4** and $^5$**8** should be related to the common energy reference point, which is **1**+external reductant. To this end, the reaction energies were computed for the following steps: $^7$**2**→$^6$**4**, which is a reduction with concomitant protonation of $Fe^{III}$–$O_2^{\bullet}$ to $Fe^{III}$–OOH (−18.4 and −18.2 kcal mol$^{-1}$ with B3LYP and B3LYP*, respectively), $^6$**4**→$^5$**8**, which corresponds to the reduction of $Fe^{III}$–OOH to $Fe^{II}$–OOH and concomitant protonation of the alcohol group of the substrate (−15.0 and −12.5 kcal mol$^{-1}$ with B3LYP and B3LYP*, respectively), and reduction plus proton uptake of $^5$**3** (**A1** in Figure 3) to the species with $Fe^{II}$–OOH and a HPP radical with a protonated alcohol group, which would be an intermediate structure between **A1** and **B2** (−11.0 and −8.6 kcal mol$^{-1}$ with B3LYP and B3LYP*, respectively). From the comparison of these values it follows that the largest driving force is for the reduction+protonation of the $Fe^{III}$–$O_2^{\bullet}$ adduct (**ES-O$_2$**→**B1**, Figure 3), whereas the smallest is for the reduction+protonation of **A1**. Since the rate for electron transfer usually correlates with the magnitude of the driving force,[32] it seems reasonable to assume that the rates of the reactions with an external reductant will follow the same trend. A common energy diagram for all three reaction mechanisms is presented in Figure 13. Even though the barriers to the electron-transfer steps are unknown, one can see that the two electron- and proton-uptake steps leading to mechanism **C** compete with initial steps of mechanisms **A** and **B** characterized by very high activation barriers ($^7$**2**→$^5$**TS1**, 26.5 kcal mol$^{-1}$ and $^6$**4**→$^6$**TS3**, 33.8 kcal mol$^{-1}$), which should favor mechanism **C**.

It should be clarified here, that since NADH is a two-electron reductant, flavin coenzyme (FMN or FAD), which is an efficient one-electron donor, is usually used in the HppE reaction in vitro. For this reason, we computed an N–H bond energy (60.6 and 61.0 kcal mol$^{-1}$ with B3LYP and B3LYP*, respectively) for a model of a fully reduced flavin coenzyme, and used this value to compute the above reaction energies for proton and electron uptakes.

**Reaction mechanisms for oxidation of (*R*)-HPP**: In the complex between HppE and (*R*)-HPP the C2-bound hydrogen is exposed towards the site of dioxygen binding, which makes this region of the HPP molecule available for a reaction.[12] What is also important is that the C2-bound oxygen binds to the active site iron in a deprotonated form, which activates the C2-O moiety towards oxidation to a ketone. In a similar way, substrates of IPNS and MIOX are "prepared" to react with iron-bound superoxides in the active sites of these enzymes.[21, 33] Indeed, such a deprotonated alcohol group can be directly two-electron oxidized to a ketone, and since this is a highly exothermic reaction, its barrier is considerably lower than for the C1–H bond activation.

From the computational results it follows that oxidation of (*R*)-HPP in the active site of HppE can be elicited either by $Fe^{III}$–$O_2^{\bullet}$ or $Fe^{IV}$=O. The key structures of the former mechanism are presented in Figure 14 A–C, whereas those for the mechanism involving $Fe^{IV}$=O are shown in Figure 14 D–F. In the transition state for the C2–H bond cleavage by the superoxo species ($^5$**TS11**) the O–O bond has a length intermediate between those observed for the superoxo and hydroperoxo groups in $^5$**18** and $^5$**19**, respectively, whereas the hydrogen atom being transferred is located closer to the destination oxygen (O2) than the parent carbon atom (C2), which is not typical for an exothermic re-

  

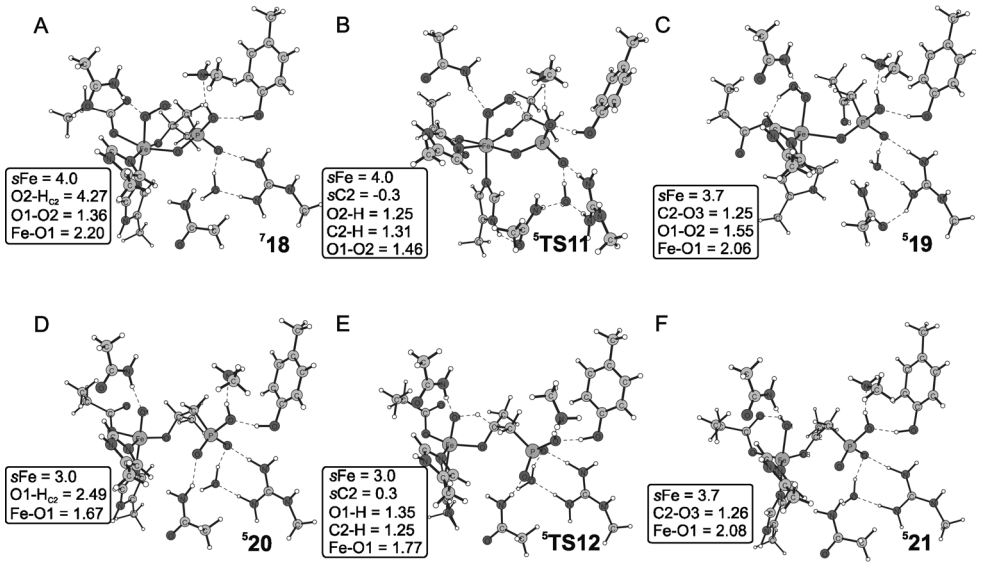


Figure 14. The key structures optimized for oxidation of (*R*)-HPP to the keto product. A–C) Structures from mechanism **A**. D–F) Structures from mechanism **C**.

action that usually has an early transition state. The barrier connected with **$^{5}$TS11** computed with B3LYP is 16.3 kcal mol$^{-1}$ (13.9 kcal mol$^{-1}$ for B3LYP*); the Fe$^{II}$–OOH/ketone product complex **$^{5}$19** lies 36.9 kcal mol$^{-1}$ (38.4 for B3LYP*) below the zero level. The barrier of 16.3 kcal mol$^{-1}$ agrees very well with the activation energy of 18.1 kcal mol$^{-1}$ (no ZPE included) computed for an analogous step in the catalytic cycle of HEPD when the substrate is assumed to be deprotonated on the hydroxyl group.[22]

The exothermicity of the C2-H cleavage step by the oxoferryl species (**$^{5}$20**→**$^{5}$TS12**→**$^{5}$21**; Figure 14 D–F) is of similar magnitude, with 39.0 and 31.7 kcal mol$^{-1}$ for B3LYP and B3LYP*, respectively. The barrier connected with **$^{5}$TS12** is also similar to that for **$^{5}$TS11**, as the B3LYP gave 13.3 kcal mol$^{-1}$, whereas B3LYP* gave 13.2 kcal mol$^{-1}$. Thus, based on the results for the current model it is not possible to unambiguously choose between the two alternative mechanisms for oxidation of (*R*)-HPP, and both of them are considered equally likely.

## Conclusion

Three different reaction scenarios for the oxidative epoxidation reaction (catalyzed by HppE and leading to fosfomycin, a clinically useful antibiotic) were probed with hybrid density functional theory (DFT) quantum chemistry methods. Based on the available crystal structure of the HppE-Fe$^{II}$-substrate (HPP) complex, a model for the active site region was constructed and used to find critical points along reaction coordinates, whose potential energies define reaction energy profiles. From a biochemical perspective, the most important result of this study is the finding that the most likely mechanism of the HppE catalytic reaction for the native (*S*)-HPP substrate involves generation of the reactive Fe$^{III}$–O$^{\bullet}$/Fe$^{IV}$=O species responsible for the C1–H bond cleavage (mechanism C, Figure 8). Interestingly, the OH-rebound, which would lead to a hydroxylated product, is prevented by a fast protonation of the Fe$^{III}$-bound hydroxyl: a strategy previously proposed for α-ketoglutarate-dependent chlorinase SyrB2.[34] From a chemical standpoint it is interesting that the O–O bond cleavage yields the Fe$^{III}$–O$^{\bullet}$ species, that is, an excited state of Fe$^{IV}$=O, and it is not unlikely that Fe$^{III}$–O$^{\bullet}$ is catalytically relevant, since it can cleave the C1–H bond without any barrier. Moreover, the barrier to the formation of the epoxide ring was found to be sensitive to the number of negatively charged ligands in the iron first coordination sphere, which must affect the redox potential of the iron ion. Oxidation of the *R* enantiomer of the substrate ((*R*)-HPP) is a single-step reaction in which the C2–H bond cleavage is performed either by Fe$^{III}$–O$_2^{\bullet}$ or the Fe$^{IV}$=O species.

## Experimental Section

**Methods**: An active site model was derived from the crystal structure in which the substrate ((*S*)-HPP) is bound to Fe$^{II}$ in a bidentate manner (PDB: 1ZZ8; Figure 2). The model involved the first shell iron ligands, that is, the side chains of His138, Glu142, His180, the whole (*S*)-HPP, and polar second shell residues: Lys23, Arg97, Tyr105, Asn135, Asn197, and a water molecule. Covalent bonds cut when selecting the active site model were saturated with hydrogen atoms and the atoms marked with asterisks in Figure 4 A were fixed during the geometry optimizations at the positions consistent with the X-ray structure. In this way the integrity of the active site model could be preserved. The active site model consisted of 107 atoms (without molecular dioxygen).

Lys23 and Arg97 were assumed to be positively charged (protonated), whereas the substrate molecule was fully deprotonated on the phosphonic acid group and also deprotonated on the C2-bound hydroxyl. Alkyl phosphonic acids have p$K_a$ values of around 2.5 and 8.0,[35] and it is expected that when the $PO_3$ group is coordinated to iron and H-bonded to

  

Arg97 and Lys23 the second p$K_a$ is shifted well below 7.0, and hence the $PO_3$ is fully deprotonated. However, during geometry optimization a proton moved from Lys23 to a nearby oxygen atom of the phosphonic group and the two groups interacted through a hydrogen bond in the majority of structures described in this work (Figure 4). This proton transfer is expected to have negligible effect on the energy results presented in this work. The above choice of protonation states together with formal charges of $Fe^{II}$ and Glu142 gave a model with a total charge equal to zero.

Geometry optimizations were performed using the hybrid density functional B3LYP and the double zeta basis set lacvp composed of the 6-31G basis for all light atoms and an effective core potential (ECP) plus double zeta basis set on iron.[36–38] Earlier experience has shown that geometries obtained with this basis set are adequate for the calculation of the final energies.[39, 40] Structures of stationary points were optimized with the Gaussian 09 suite of programs,[41] whereas the software package Jaguar 7 was used for the calculation of the final DFT electronic energies.[42]

Transition states were searched for in the following way. First, a relaxed scan was performed for an approximate reaction coordinate, such as a selected interatomic distance. Second, for the geometry corresponding to the maximum energy along the calculated profile, a molecular Hessian was computed and then used in the subsequent full optimization of the transition state performed with the Berny algorithm implemented in Gaussian.[41] The character of the optimized structure was checked with a frequency analysis. For all transition states it was found that there existed one normal mode with an imaginary frequency describing passage over the barrier. Values of these frequencies are provided in the Supporting Information.

Stability of the results with respect to variations of the exchange-correlation functional was checked with single-point calculations employing B3LYP*, that is, with a reduced amount of Hartree–Fock like exchange (from 20 to 15%). Large differences between relative energies computed with B3LYP and B3LYP* are supposed to be diagnostic for cases in which these functionals may fail to provide reliable energies.

B3LYP and B3LYP* electronic energies were calculated using the cc-pVTZ(-f) basis set (without f-functions) on all atoms of main group elements. For iron a triple zeta basis set supplemented with diffuse functions, that is, lacv3p+, was employed.

To account for the polarization effects of the solvent, the self-consistent reaction field (SCRF) method implemented in Jaguar was used.[43, 44] In the SCRF method, the solvent is described as a polarizable dielectric continuum, in which the solute is contained in a solute-shaped cavity. The solvent is defined by the dielectric constant $\varepsilon$, which is taken to be 4.0 for the buried active sites in the metalloenzymes and 80.37 for water.

The reported final energies combine the electronic energy calculated at the B3LYP (B3LYP*)/cc-pVTZ(-f),lacv3p+ level, with the solvent and zero point energy corrections calculated at the B3LYP/lacvp level and with the van der Waals empirical correction.[45]

Minimum energy crossing points (MECP) between two non-interacting potential energy surfaces were optimized with the use of the meta-program Crossing obtained by courtesy of Prof. J. Harvey.[46] In these computations the basis set lacv3p+ was used for iron, whereas the first shell atoms were described with the cc-pVTZ(-f) basis. For other atoms the standard lacvp basis set was used. The two minima connected by a given MECP were also re-optimized in this extended basis, and their final energies were compared to that obtained for MECP.

The spin populations reported are used to monitor changes in the spin and oxidation states, and were derived from the Mulliken population analysis.

## Acknowledgements

We are grateful to Sven de Marothy for providing us with his XYZ-Viewer program, which was used to produce molecular graphics and also calculate vdW energy corrections. This research project was supported by grant No. UMO-2011/01/B/ST4/02620 from the National Science Centre, Poland. A. M. has been partly supported by the EU Human Capital Operation Program, Polish Project No. POKL.04.0101-00-434/08-00.

[1] P. Liu, K. Murakami, T. Seki, X. He, S. M. Yeung, T. Kuzuyama, H. Seto, H. Liu, *J. Am. Chem. Soc.* **2001**, *123*, 4619–4620.
[2] F. Hammerschmidt, H. Kahlig, *J. Org. Chem.* **1991**, *56*, 2364–2370.
[3] F. Hammerschmidt, *J. Chem. Soc. Perkin Trans. 1* **1991**, 1993–1996.
[4] B. Peric Simov, F. Wuggenig, M. Lämmerhofer, W. Lindner, E. Zarbl, F. Hammerschmidt, *Eur. J. Org. Chem.* **2002**, *2002*, 1139–1142.
[5] Z. Zhao, P. Liu, K. Murakami, T. Kuzuyama, H. Seto, H. wen Liu, *Angew. Chem.* **2002**, *114*, 4711–4714; *Angew. Chem. Int. Ed.* **2002**, *41*, 4529–4532.
[6] P. Liu, A. Liu, F. Yan, M. Wolfe, J. Lipscomb, H. Liu, *Biochemistry* **2003**, *42*, 11577–11586.
[7] F. Yan, J. W. Munos, P. Liu, H. wen Liu, *Biochemistry* **2006**, *45*, 11473–11481.
[8] P. Liu, M. P. Mehn, F. Yan, Z. Zhao, L. Que, H. wen Liu, *J. Am. Chem. Soc.* **2004**, *126*, 10306–10312.
[9] L. M. Mirica, K. P. McCusker, J. W. Munos, H. wen Liu, J. P. Klinman, *J. Am. Chem. Soc.* **2008**, *130*, 8122–8123.
[10] L. J. Higgins, F. Yan, P. Liu, H. wen Liu, C. L. Drennan, *Nature* **2005**, *437*, 838–844.
[11] E. Hegg, L. Que Jr., *Eur. J. Biochem.* **1997**, *250*, 625–629.
[12] D. Yun, M. Dey, L. J. Higgins, F. Yan, H. wen Liu, C. L. Drennan, *J. Am. Chem. Soc.* **2011**, *133*, 11262–11269.
[13] F. Yan, S.-J. Moon, P. Liu, Z. Zhao, J. D. Lipscomb, A. Liu, H. wen Liu, *Biochemistry* **2007**, *46*, 12628–12638.
[14] J. M. Bollinger, C. Krebs, *Curr. Opin. Chem. Biol.* **2007**, *11*, 151–158.
[15] M. S. Chow, L. V. Liu, E. I. Solomon, *Proc. Natl. Acad. Sci. USA* **2008**, *105*, 13241–13245.
[16] N. Lehnert, R. Y. Ho, L. Que, E. I. Solomon, *J. Am. Chem. Soc.* **2001**, *123*, 12802–12816.
[17] A. Bassan, M. R. A. Blomberg, T. Borowski, P. E. M. Siegbahn, *J. Inorg. Biochem.* **2006**, *100*, 727–743.
[18] S. P. de Visser, *Iron-Containing Enzymes. Versatile Catalysts of Hydroxylation Reactions in Nature* (Eds.: S. P. de Visser, D. Kumar), RCS Publishing, Cambridge, UK, **2011**, pp. 1–41.
[19] T. Borowski, A. Bassan, P. E. M. Siegbahn, *Biochemistry* **2004**, *43*, 12331–12342.
[20] A. Bassan, T. Borowski, P. E. M. Siegbahn, *Dalton Trans.* **2004**, *20*, 3153–3162.
[21] M. Lundberg, P. Siegbahn, K. Morokuma, *Biochemistry* **2008**, *47*, 1031–1042.
[22] H. Hirao, K. Morokuma, *J. Am. Chem. Soc.* **2010**, *132*, 17901–17909.
[23] S. Aluri, S. P. de Visser, *J. Am. Chem. Soc.* **2007**, *129*, 14846–14847.
[24] D. Kumar, W. Thiel, S. P. de Visser, *J. Am. Chem. Soc.* **2011**, *133*, 3869–3882.
[25] F. Ogliaro, S. P. de Visser, S. Cohen, P. K. Sharma, S. Shaik, *J. Am. Chem. Soc.* **2002**, *124*, 2806–2817.
[26] E. Derat, D. Kumar, H. Hirao, S. Shaik, *J. Am. Chem. Soc.* **2006**, *128*, 473–484.
[27] P. J. Riggs-Gelasco, J. C. Price, R. B. Guyer, J. H. Brehm, E. W. Barr, J. M. Bollinger, C. Krebs, *J. Am. Chem. Soc.* **2004**, *126*, 8108–8109.
[28] M. Lundberg, T. Borowski, *Coord. Chem. Rev.* **2012**, *256*, DOI: 10.1016/j.ccr.2012.03.047.
[29] M. L. Neidig, A. Decker, O. W. Choroba, F. Huang, M. Kavana, G. R. Moran, J. B. Spencer, E. I. Solomon, *Proc. Natl. Acad. Sci. USA* **2006**, *103*, 12966–12973.
[30] K. McLuskey, S. Cameron, F. Hammerschmidt, W. N. Hunter, *Proc. Natl. Acad. Sci. USA* **2005**, *102*, 14221–14226.
[31] W. Humphrey, A. Dalke, K. Schulten, *J. Mol. Graph.* **1996**, *14*, 33–38.

  

[32] R. Marcus, N. Sutin, *Biochim. Biophys. Acta Rev. Bioenerg.* **1985**, *811*, 265–322.
[33] G. Xing, Y. Diao, L. M. Hoffart, E. W. Barr, K. S. Prabhu, R. J. Arner, C. C. Reddy, C. Krebs, J. M. Bollinger, *Proc. Natl. Acad. Sci. USA* **2006**, *103*, 6130–6135.
[34] S. Pandian, M. A. Vincent, I. H. Hillier, N. A. Burton, *Dalton Trans.* **2009**, 6201–6207.
[35] D. Martin, C. Griffin, *J. Organomet. Chem.* **1964**, *1*, 292–296.
[36] A. D. Becke, *Chem. Phys.* **1993**, *98*, 5648–5652.
[37] C. Lee, W. Yang, R. G. Parr, *Phys. Rev.* **1988**, *B37*, 785–789.
[38] P. Hay, W. Wadt, *J. Chem. Phys.* **1985**, *82*, 299–310.
[39] P. E. M. Siegbahn, *J. Comput. Chem.* **2001**, *22*, 1634–1645.
[40] P. E. M. Siegbahn, T. Borowski, *Acc. Chem. Res.* **2006**, *39*, 729–738.
[41] Gaussian 09, Revision A.2, M. J. Frisch, G. W. Trucks, H. B. Schlegel, G. E. Scuseria, M. A. Robb, J. R. Cheeseman, G. Scalmani, V. Barone, B. Mennucci, G. A. Petersson, H. Nakatsuji, M. Caricato, X. Li, H. P. Hratchian, A. F. Izmaylov, J. Bloino, G. Zheng, J. L. Sonnenberg, M. Hada, M. Ehara, K. Toyota, R. Fukuda, J. Hasegawa, M. Ishida, T. Nakajima, Y. Honda, O. Kitao, H. Nakai, T. Vreven, J. A. Montgomery, Jr., J. E. Peralta, F. Ogliaro, M. Bearpark, J. J. Heyd, E. Brothers, K. N. Kudin, V. N. Staroverov, R. Kobayashi, J. Normand, K. Raghavachari, A. Rendell, J. C. Burant, S. S. Iyengar, J. Tomasi, M. Cossi, N. Rega, J. M. Millam, M. Klene, J. E. Knox, J. B. Cross, V. Bakken, C. Adamo, J. Jaramillo, R. Gomperts, R. E. Stratmann, O. Yazyev, A. J. Austin, R. Cammi, C. Pomelli, J. W. Ochterski, R. L. Martin, K. Morokuma, V. G. Zakrzewski, G. A. Voth, P. Salvador, J. J. Dannenberg, S. Dapprich, A. D. Daniels, Ö. Farkas, J. B. Foresman, J. V. Ortiz, J. Cioslowski, D. J. Fox, Gaussian Inc. Wallingford CT **2009**.
[42] *JAGUAR 7*, Schrödinger, Inc., Portland, Oregon, **2007**.
[43] D. J. Tannor, B. Marten, R. Murphy, R. A. Friesner, D. Sitkoff, A. Nicholls, M. Ringnalda, W. A. Goddard III, B. Honig, *J. Am. Chem. Soc.* **1994**, *116*, 11875–11882.
[44] B. Marten, K. Kim, C. Cortis, R. A. Friesner, R. Murphy, M. Ringnalda, D. Sitkoff, B. Honig, *J. Phys. Chem.* **1996**, *100*, 11775–11788.
[45] S. Grimme, *J. Comput. Chem.* **2006**, *27*, 1787–1799.
[46] J. N. Harvey, M. Aschi, H. Schwarz, W. Koch, *Theor. Chem. Acc.* **1998**, *99*, 95–99.

Received: August 6, 2012
Published online: November 13, 2012

  